IBRACON Structures and Materials Journal
Revista IBRACON de Estruturas e Materiais
ISSN 1983-4195 ismj.org

ORIGINAL ARTICLE

Numerical analysis of crack opening on flat slabs exposed to fire: spring stiffness and displacement rate influence

Análise numérica da abertura de fissuras em lajes lisas expostas ao fogo: influência da rigidez de mola e da taxa de deslocamento

Andreia Romero Fanton[a]
Luiz Carlos de Almeida[a]
Leandro Mouta Trautwein[a]

[a]Universidade Estadual de Campinas – UNICAMP, Departamento de Estruturas, Campinas, SP, Brasil

Received 18 december 2025
Revised 17 August 2026
Accepted 23 September 2026

Abstract: Though much information has been gathered on punching shear on slabs in a fire scenario, there remains a need for a broader understanding of the displacement rate influence on the crack opening behavior. To understand the load influence on crack opening in concrete flat slabs under fire conditions, computer modelling tools were applied, based on Non-Linear Finite Element Analysis (NLFEA). A detailed calibration was carried out to obtain the optimal spring stiffness for the final numerical model based on experimental results from the literature. The influence of spring stiffness on the structural behaviour of flat slabs subjected to fire exposure remains a scarcely investigated topic. The study parameters were *spring stiffness* and *displacement rate.* The applied load was then varied to compare the crack pattern and the crack propagation speed in the heated slab. Displacement rates (DR) were increased in increments of 0.2 mm/min, while keeping the same number of steps. Analysis of the models showed that the slab loaded at 1.0 mm/min presented 3.19 mm-cracks immediately before failure, while the slab loaded at 0.6 mm/min exhibited 2.81 mm-cracks, and the slab loaded at 0.2 mm/min presented 1.85 mm-cracks. Overall, the results demonstrate that the displacement rate has a direct influence on the cracking behaviour of flat slabs exposed to fire. Higher displacement rates produced larger crack widths before failure, reflecting a more brittle structural response, whereas lower rates resulted in smaller cracks and a more gradual progression toward collapse. These outcomes emphasize the need for precise spring-stiffness calibration and careful selection of loading parameters in numerical modelling, as both play a crucial role in accurately predicting slab performance in fire conditions.

Keywords: concrete, fire, finite elements, crack opening, flat slabs.

Resumo: Embora existam muitas informações sobre punção em lajes em situação de incêndio, ainda há necessidade de uma compreensão mais ampla da influência da taxa de deslocamento no comportamento da abertura de fissuras. Para entender a influência da carga na abertura de fissuras em lajes lisas de concreto em incêndio, foram aplicadas ferramentas de modelagem computacional, baseadas na Análise Não-Linear de Elementos Finitos (NLFEA). Uma calibração extensa foi feita para obter a melhor rigidez de mola para o modelo numérico final em comparação com resultados experimentais da literatura. A influência da rigidez da mola no comportamento estrutural de lajes planas expostas ao fogo permanece um tema pouco explorado. Os parâmetros do estudo foram a rigidez de mola e a taxa de deslocamento. As taxas de deslocamento (DR) foram aumentadas em incrementos de 0,2 mm/min, mantendo-se o número de etapas. A análise dos modelos mostrou que a laje carregada a 1,0 mm/min apresentou fissuras de 3,19 mm imediatamente antes da ruptura, enquanto a laje carregada a 0,6 mm/min apresentou fissuras de 2,81 mm, e a laje carregada a 0,2 mm/min apresentou fissuras de 1,85 mm. No geral, os resultados demonstram que a taxa de deslocamento exerce influência direta no comportamento de fissuração de lajes lisas expostas ao fogo. Taxas de deslocamento mais altas produziram maiores aberturas de fissuras antes da ruptura, refletindo uma resposta estrutural mais frágil, enquanto taxas menores resultaram em fissuras menores e uma progressão mais gradual em direção ao colapso. Esses resultados destacam a necessidade de uma calibração precisa da rigidez de mola e de uma seleção detalhada dos parâmetros de carregamento na modelagem numérica, pois ambos desempenham papel fundamental na previsão do desempenho das lajes em condições de incêndio.

Palavras-chave: concreto, fogo, elementos finitos, abertura de fissuras, lajes lisas.

How to cite: A. R. Fanton, L. C. Almeida, and L. M. Trautwein, "Numerical analysis of crack opening on flat slabs exposed to fire: spring stiffness and displacement rate influence," *Rev. IBRACON Estrut. Mater.*, vol. 19, no. 4, e19406, 2026, https://doi.org/10.1590/S1983-41952026000400006

Corresponding author: Andreia Romero Fanton. E-mail: a145318@dac.unicamp.br
Financial support: The authors greatly appreciate the financial support provided by Coordenação de Aperfeiçoamento de Pessoal de Nível Superior (CAPES).
Conflict of interest: Nothing to declare.
Data Availability: The data that support the findings of this study are available from the corresponding author, [ARF], upon reasonable request. "SciELO Data" is

This is an Open Access article distributed under the terms of the Creative Commons Attribution license (https://creativecommons.org/licenses/by/4.0/), which permits unrestricted use, distribution, and reproduction in any medium, provided the original work is properly cited.

1 INTRODUCTION

Although several studies have been conducted on punching in flat slabs, the number of studies that simulate the fire performance of slabs subjected to this type of failure is scarce. In the last few decades, associated with experimental research, numerical analyses have also been developed using the Finite Element Method (FEM). For the study of punching shear, this analysis is very useful, given that carrying out experimental tests on slabs is expensive and challenging to perform.

Flat slabs are widely used in underground structures, such as car parks, due to their large surface area, static efficiency, and large span-depth ratios. Major car park fires are becoming increasingly common, as seen in the Liverpool Echo Arena incident in 2017, and the car park at Luton Airport on 10 October 2023, which was built just four years earlier. The Luton London car park fire was caused by a vehicular fault that started from a diesel-powered car. There were more than 1,400 cars parked at the time of the incident.

Though considerable information has been gathered on punching shear on slabs in a fire scenario, there remains a need for a broader understanding of the crack opening response of flat slabs subjected to fire exposures. In this research, the effects of the displacement rate on the punching shear response of flat slabs were analysed by applying non-linear temperature-dependent properties to the reinforced concrete. The load applied was changed to compare the crack pattern and the crack propagation speed on the heated slab. The motivation on this study is the impact that the support condition has on the punching shear failure, and the lack on the studies on unrestrained flat slabs in fire situations. The influence of spring stiffness on the structural behaviour of flat slabs subjected to fire exposure remains a scarcely investigated topic within the literature. The specific role of boundary condition flexibility, which is represented through spring stiffness, has received limited attention. This research gap is of considerable importance, as the stiffness of supports can substantially affect load redistribution mechanisms, deflection patterns, and failure modes during fire exposure. Consequently, a more comprehensive investigation into the effects of spring stiffness is essential to enhance the accuracy and realism of structural fire performance assessments for flat slab systems. Computer modelling tools were applied, based on Non-Linear Finite Element Analysis (NLFEA).

2 THEORETICAL BACKGROUND

2.1 Flat slabs in fire situation

The structural system called flat slabs consists of reinforced or prestressed concrete slabs that are supported directly on columns. This system has a complex structural behavior, especially in slab-column connections, where punching failure can occur due to shear stress [1]. The serviceability limit state (possible large deflections) and the ultimate limit state (punching shear) are the crucial factors that limit the slenderness and determine the thickness of a flat slab [2].

Two fail mechanisms can happen in reinforced concrete structures: flexural and shear. Flexural failure is a ductile failure, characterized by the formation of visible tensile cracks prior to failure. Shear failure is a brittle failure; it occurs with slight displacement or a few crack warning signs [3]. Punching shear failure happens when a column punches the slab that it is supporting, leading to a cone crack pattern (Figure 1).

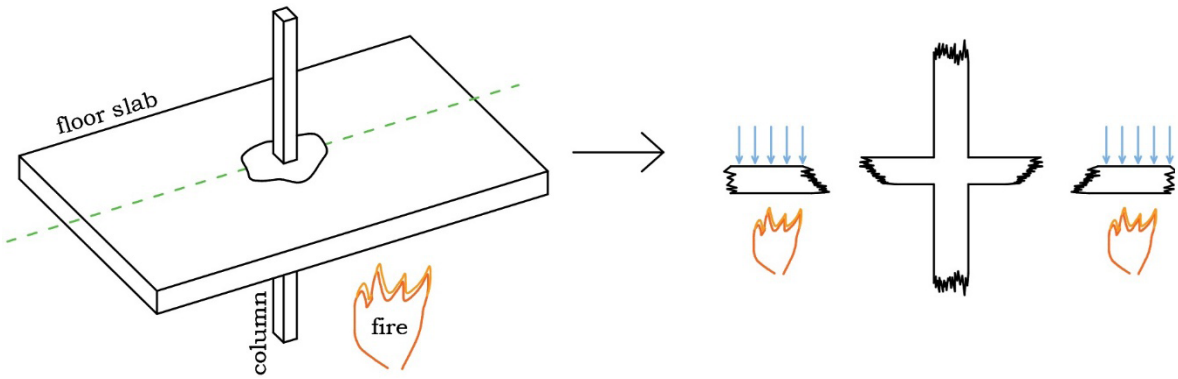


Figure 1. Punching shear (adapted from Smith [3])

Smith [3] studied the effects of restrained thermal expansion in flat slabs by altering the support conditions of slab-column. A comparison was made between unrestrained and restrained support condition. The support condition was shown to have a significant impact on the punching shear failure. The unrestrained slabs failed soon after heating started, whereas the equivalent restrained slabs had a high comparative residual strength. Additionally, the restrained support condition significantly decreased the central vertical displacement. Punching shear in RC slabs at elevated temperatures depends on the effects of steel and concrete properties in fire, material thermal expansion differences, and the structural effects of in-plane actions resulting from restrained thermal expansion, as well as large deflection load-carrying mechanisms [3].

According to Smith [3], the higher residual strength observed in restrained slabs is primarily attributed to the development of compressive membrane action resulting from restrained thermal expansion. When in-plane expansion is prevented, compressive forces are generated within the slab, enhancing its load-carrying capacity by reducing tensile stresses and redistributing internal forces away from the slab–column connection.

This mechanism becomes particularly beneficial under elevated temperatures, where material degradation would otherwise govern the response. Unrestrained slabs are free to expand and therefore do not develop these compressive forces, resulting in a response dominated by the loss of stiffness and strength, and consequently leading to earlier punching shear failure.

2.2 Effect of elevated temperature on concrete

Concrete is a heterogeneous material, and its behavior, when exposed to high temperatures (above 60 °C), is of great complexity. The models representing the properties as a function of temperature rise are elaborated through average curves. These curves are established by results of experiments or numerical modeling [4]. The concrete model used is based on the fracture-plastic model. For concrete, the temperature-dependent concrete properties were based on Eurocode 2 (EN 1992-1-2:2023) [5].

Anderberg and Thelandersson [6] proposed a concrete constitutive law for high-temperature conditions in transient regimes, based on the experiments performed. For the formulation to be as adequate as possible, the total strain is given as the sum of four different parcels, each related to a different test, as follows: thermal strain (including shrinkage, measured on unstressed specimens under variable temperature); instantaneous stress-related strain (based on stress-strain curves obtained under constant temperature); creep-strain (time-dependent strain, measured under constant temperature); transient strain (responsible for the increase temperature effect under stress, obtained from tests under constant stress and variable temperature).

The law can be expressed as the Equation 1:

$$\varepsilon_T = \varepsilon_{th}\left(T\right) + \varepsilon_{\sigma}\left(\tilde{\sigma},\sigma,T\right) + \varepsilon_{cr}\left(\sigma,T,t\right) + \varepsilon_{tr}\left(\sigma,T\right) \quad (1)$$

where: ε_T = total strain (%); ε_{th} = thermal strain (%); ε_{σ} = stress-related strain (%); ε_{cr} = creep strain (%); ε_{tr} = transient strain (%); T = temperature; σ = stress (kN/cm^2); $\tilde{\sigma}$ = stress history (kN/cm^2); and t = time (s).

A detailed description of each parcel can be found in Fanton [7]. The modulus of elasticity (E_c), critical compressive displacement (W_d), plastic strain at peak compressive stress (ε_{cp}), f_c' (compressive strength) and ε_{th} (thermal strain) coefficients were determined by applying temperature-dependent reduction factors, as defined in Eurocode 2 (EN 1992-1-2) [5], to their respective values at ambient temperature. There is an interrelationship between density and thermal expansion. Most solid materials expand when heated, and contract when cooled, i.e., there is a change in volume that acts on the density [4]. At high temperatures, there is a reduction in the concrete density due to the evaporation of water that is free in the material, and the increase in volume caused by thermal expansion.

Due to the restrictions imposed by thermal dilatation, thermal elongation is crucial for the analysis of 2nd order effects, especially when frames are modelled. In the case of isolated elements, it can also be convenient for simplified calculation methods. The elongation is determined through the relationship between the elongation that occurs with the increase in temperature and the initial length of the element - this being at a temperature of 20 °C, with restricted axial displacement [8].

The concrete model is based on the fracture-plastic model. For concrete, the temperature-dependent concrete properties [thermal conductivity (k_c - W/m°C), specific heat capacity (ρ_c), density (ρ), compressive strength (f_c') and thermal expansion strain (ε_{th})] are based on Eurocode 2 (EN 1992-1-2:2023) [5]. The modulus of elasticity (E_c), critical compressive displacement (W_d), plastic strain at peak compressive stress (ε_{cp}), f_c' and ε_{th} coefficients are considered multiplied to the initial value of the parameters at normal temperatures and are shown in Figures 2a, 2b, 2c and 2d.

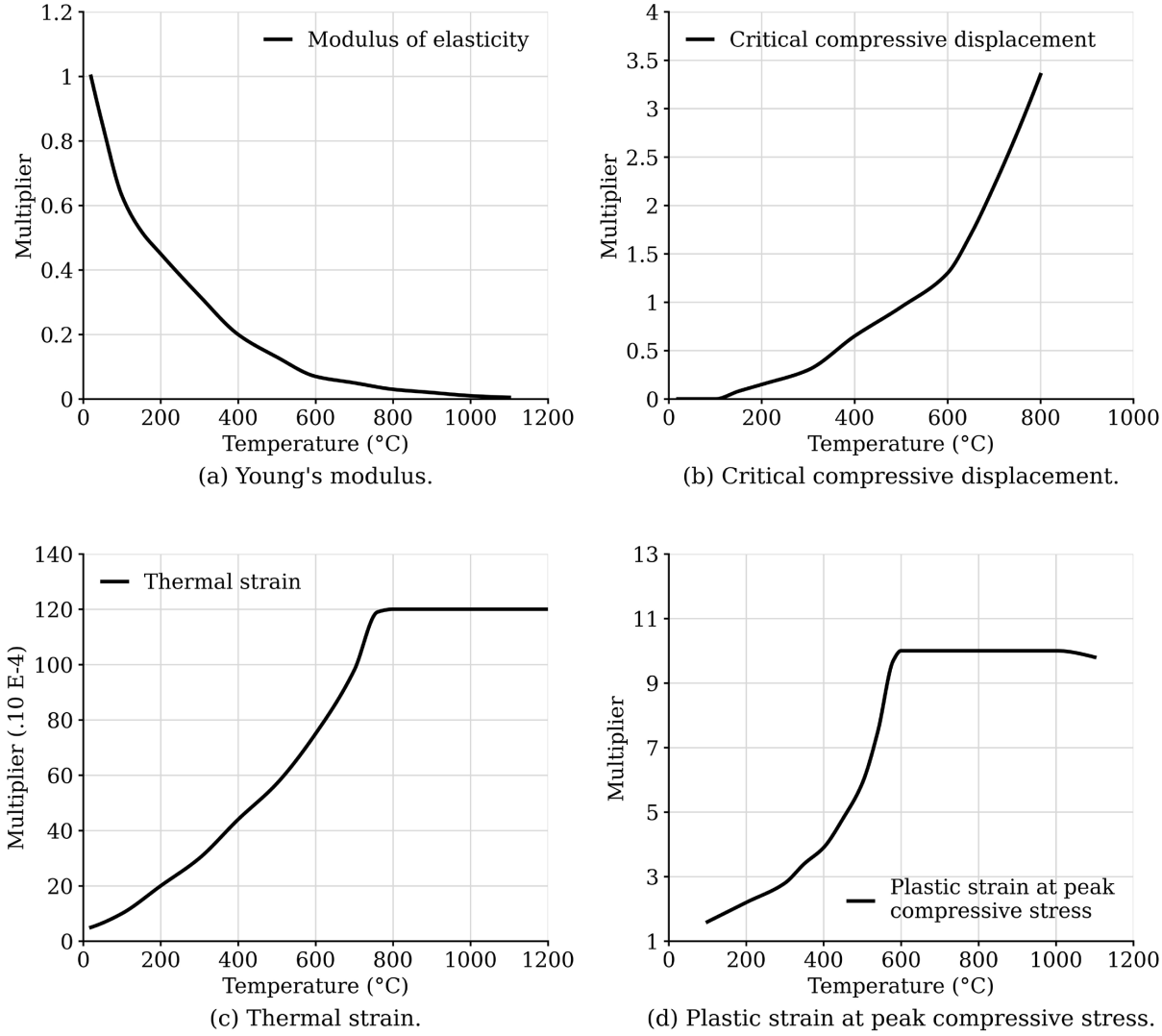


Figure 2. Concrete properties (Adapted from Sadaghian and Farzam [9]).

As the temperature rises, the compressive strength decreases progressively, leading to a reduction in both stiffness and load-carrying capacity. This degradation was considered in the numerical model through temperature-dependent factors based on Eurocode 2 (EN 1992-1-2:2023) [5]. In Figure 2, although not explicitly shown, this reduction directly influences the observed behaviour. The decrease in compressive strength contributes to earlier cracking, increased deformability, and a lower ultimate load.

For concrete, the thermal conductivity is reduced with the rise in temperature, and is related to the aggregate used, in addition to the porosity of the cement paste. Through dehydration of concrete, the tendency is that this property reduces with increasing temperature.

Specific heat is a property defined as the amount of heat required to raise the material temperature by one degree in one unit of mass. The specific heat unit is Joule per kilogram and degree Celsius [J/(kg°C)]. There are three different functions for determining the concrete specific heat, considering that there is a constant peak value for temperatures between 100 °C and 115 °C, according to EN 1992-1-2:2023 [5]. The existence of this peak is related to the water evaporation that is free inside the concrete.

In fire resistance tests, the temperature rise is typically defined by standardized fire curves to ensure consistency and comparability between different studies. The most commonly adopted is the ISO 834 standard fire curve, which represents a conventional time-temperature relationship for structural fire exposure and is widely used in both experimental and numerical analyses.

2.3 Cracking

Concrete thermal expansion and dehydration caused by heating may lead to the formation of cracks in the concrete in addition to spalling. These fissures may provide pathways for direct heating of the reinforcement bars, possibly bringing about more thermal stress and further cracking. Depending on the circumstances, the cracks provide pathways for hot combustion products to spread through the barrier to the adjoining compartment. Generally, the cracks extended quite deep within the concrete member [10]. Stress concentrations near cracks are critical in the slab-column region, as they govern crack propagation and contribute to the development of punching shear failure.

The determination of stresses and displacements for various crack problems is done through complex variable methods. In 1937, Westergaard [11] developed a complex variable method to determine stresses around cracks. Westergaard's solution is applied directly to cracks, without the need to approximate the crack at its limit by an ellipse. It is also expressed in rectangular coordinates. This method uses the so-called Westergaard stress function.

According to Sadd [12], crack problems in elasticity lead to singularities and discontinuities with two important characteristics. Firstly, the nature of the stresses at the crack tip, especially their singularity. The second characteristic is due to the displacements along the crack surface, which are often multivalued. Once the crack appears in the structure, it can propagate.

Fanton *et al.* [13] investigated the effect of load on crack opening in concrete flat slabs under fire conditions using Nonlinear Finite Element Analysis (NLFEA) with ATENA software and the GiD preprocessor, focusing on applied load and displacement rate.

Concrete flat slab-column connections are susceptible to punching failure. A premature collapse can occur during fire caused by the increase of the punching load due to the thermal curvatures' restraint. Annerel *et al.* [14] analyzed the axial load increase on a column owing to the restrained thermal elongations and curvatures. They carried out a thermo-mechanical model of an underground car park structure using ABAQUS. The highest axial load increase was found when the modulus of elasticity is kept constant at its initial value.

3 EXPERIMENTAL TEST

3.1 Geometry of the test and boundary conditions

This section will present the experimental results obtained by Smith [3] which will be used to calibrate the finite element model in this study. Among the flat slabs studied by her, AU-100/0.8 (ambient temperature, unrestrained, 100 mm thickness with 0.8% reinforcement ratio) and HU-100/0.8 (heated, unrestrained, 100 mm thickness with 0.8% reinforcement ratio). The cylinder and cube compression and split-cylinder tension tests were undertaken from the slab-column specimen testing performed by Smith [3]. The ambient characteristic compressive cylinder concrete strength was an average of 51 MPa at 28 days, as presented in Figure 3.

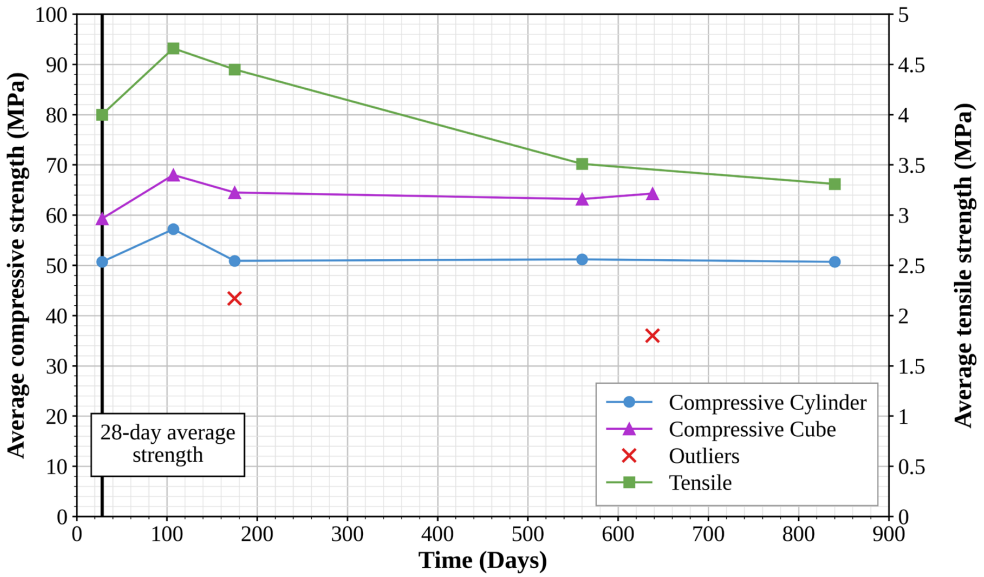


Figure 3. Concrete compressive and tensile strength versus time (adapted from Smith [3])

The flat slabs were 1400x1400x100 mm 0.8% reinforced, and a central column of 120x120x100 mm. No shear reinforcement was used to ensure shear failure. The flat slabs were tested using a 2mm/min displacement rate. The sustained load applied during heated tests was taken as 70% of the ambient capacity from the ambient test results, according to Eurocode 2 (EN 1992-1-2:2023) [5]. The slab-column specimen design by Smith [3] was based on ambient testing by Guandalini *et al.* [15], to ensure the failure mode was punching shear. The slabs modelled in this present work are presented in Table 1.

Table 1. Specimen details

SPECIMEN ID	FIRE SCENARIO	SLAB DIMENSION (mm x mm x mm)	REINF. RATIO (%)	REINF. DIAMETER (mm)	REINF. SPACING (mm)	MOISTURE CONTENT (%)
AU-100/0.8	Ambient	1400 x 1400 x 100	0.8	6	42	4
HU-100/0.8	Heated	1400 x 1400 x 100	0.8	6	42	4

The reinforcement layout consisted of 33 ϕ6mm longitudinal steel bars and 33 ϕ6mm secondary reinforcement steel bars. The spacing was 42mm. The concrete cover was 9mm thick vertically and 7 mm thick on the slab sides. In the compression area, two bars were placed to tie the column stub to the slab in accordance with BS EN 1992-1-1:2023 [16]. The two bars also prevent unzipping of the reinforcement during failure and spanned in the same direction as the orientation of the flexural reinforcement. Figure 4 presents the full reinforcement schedule for the unrestrained 100 mm thick slab with 0.8% reinforcement ratio.

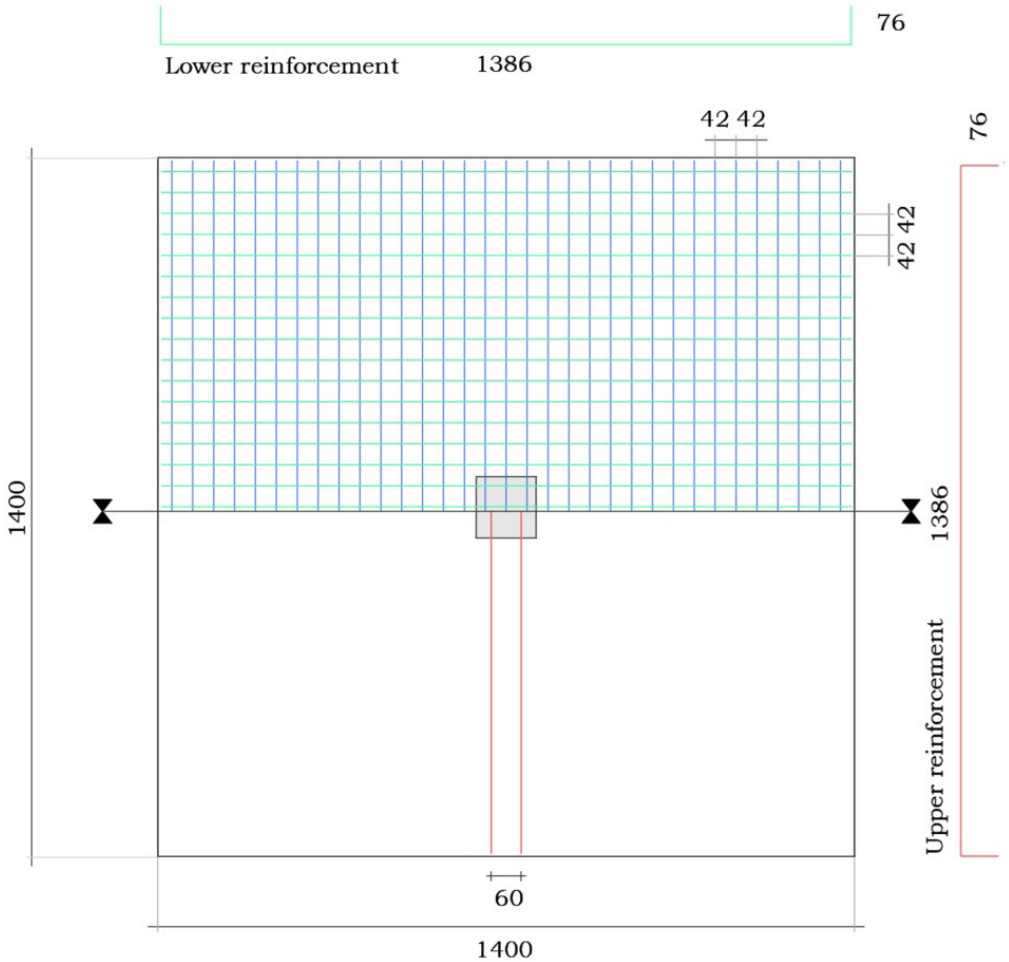


Figure 4. Reinforcement schedule – 100 mm thick slab 0.8% reinforcement ratio (in mm)

The column reinforcement consists of eight ϕ4 mm steel bars. In the experimental model by Smith [3], a 2.5x2.5 mm galvanised steel mesh was used to increase the column stub capacity and ensure the column did not crush prior to slab failure. The column stub did not fail prior to slab failure in any test. Figure 5 presents the column reinforcement schedule.

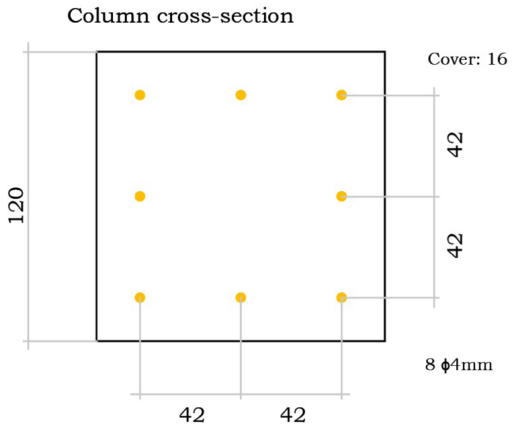


Figure 5. Column cross-section (units in mm)

Figure 6 shows the unrestrained condition was achieved by supporting the slab on a 6mm diameter steel rod. The rod was temporarily held in place with Blu-tack on the box section, which was horizontally bolted to the structural reaction frame. A 5 mm gap between the slab edge and structural reaction frame was created to allow the slab to freely rotate and expand.

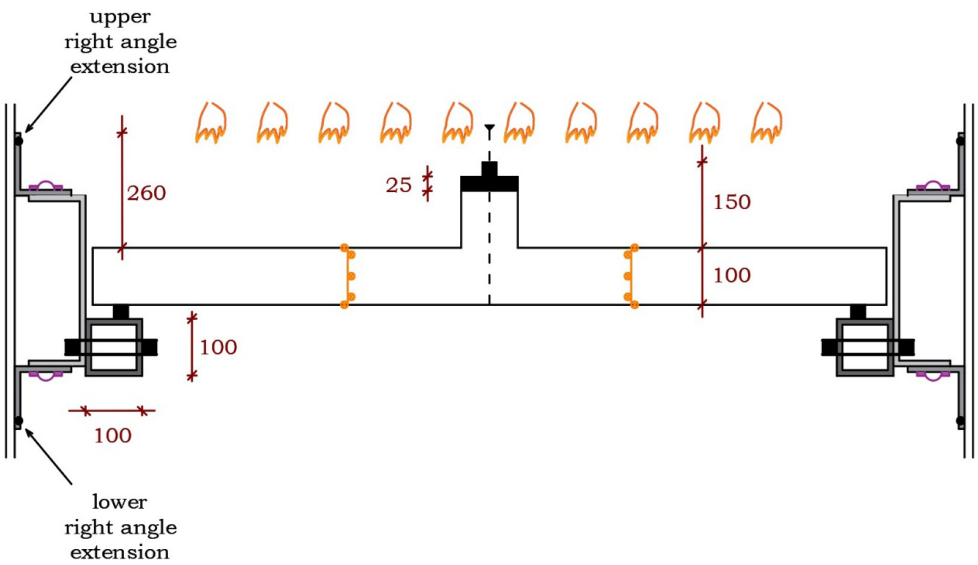


Figure 6. Structural reaction frame (adapted from Smith [3])

Experimental investigations, such as those by Annerel *et al.* [14] punching shear tests, demonstrated that fire exposure leads to a reduction in punching capacity due to material degradation, while simultaneously inducing additional forces caused by restrained thermal deformations.

Several studies have investigated the behaviour of reinforced concrete flat slabs and slab column connections under fire conditions, focusing on punching shear resistance and thermo-mechanical response. Experimental works have shown that elevated temperatures significantly reduce load-bearing capacity and modify failure mechanisms due to material degradation and restrained thermal deformations. Numerical and analytical studies have emphasized the importance of accurately representing thermal gradients, boundary conditions, and temperature-dependent material properties in predicting structural behaviour.

Despite these contributions, the available literature remains limited, particularly regarding fully calibrated thermo-mechanical models and the influence of boundary conditions, such as support flexibility, on slab response under fire. This gap motivates the present study.

In the experimental model conducted by Smith [3], two linear potentiometers were attached to a 600 kN hollow jack to measure the jack extension, assumed to be equal to the column displacement. Additionally, three cameras were used for measuring vertical displacement.

3.2 Materials properties

3.2.1 Concrete

The concrete grade used by Smith [3] was RC40/50, with a maximum aggregate size of 10mm. The ambient characteristic compressive cylinder concrete strength was measured to be an average of 51 MPa at 28 days. Ready-mix concrete was used so that all the slab-column and concrete strength specimens could be cast from the same batch. Siliceous aggregate was used. The measured slump was 130 mm.

3.2.2 Reinforcement

Table 2 presents the average material properties of reinforcement of each flat slab model, where f_y is the yield strength of flexural reinforcement, m_R is the nominal moment capacity per unit width, E_S is the modulus of elasticity of reinforcement, and V_{flex} is the shear force associated with the flexural capacity of the slab specimen.

Table 2. Mechanical properties of reinforcement

SPECIMEN ID	REINFORCEMENT DIAMETER (mm)	f_y (MPa)	m_R (N)	E_S (GPa)	V_{flex} (KN)
AU-100/0.8	6	550	29500	200	224
HU-100/0.8	6	549	28800	200	219

The flexural reinforcements were composed of bars distributed at the upper and lower slab faces. The reinforcement steel was ribbed, cold worked.

3.3 Overview of the test results

The experiments performed by Smith [3] had the following results:

- The maximum approximate concrete temperature near the heated surface was 130 ºC;
- The flexural steel at an effective depth of 81 mm reached an approximate average maximum temperature of 18 ºC;
- Slab failed in punching shear mechanisms; and
- The ambient temperature tested slab had a capacity of 226.3 kN. The specimen was loaded to 174.6 kN during heating.

4 NONLINEAR NUMERICAL MODELLING

Nonlinear finite element analyses (NLFEA) are a useful tool for investigating and predicting the behavior of reinforced concrete structures. Here, the heat transfer analysis implemented in ATENA [17] is applied to study the slab behavior.

4.1 Constitutive models

The ATENA program (Advanced Tool for Engineering Nonlinear Analysis) is based on the Finite Element Method and was developed by the company Cervenka Consulting. The GiD preprocessor allows the construction of model geometry, the definition of material properties, load conditions and its history by defining finite element intervals and meshes, to perform static analysis and heat conduction calculations (transport analysis). The models of these two analyzes are not identical, but compatible. The finite element mesh is different, but the temperatures for the static analysis are inferred from the temperatures associated with the mesh used in the thermal analysis.

For brittle materials, such as concrete, ATENA uses a fracture-plastic constitutive model called Fracture-Plastic Constitutive Model, which combines fracture in tension with plasticity in compression. Concrete fracture is based on the classical formulation of the smeared crack [18] and the crack band model [19]. Crack propagation is based on the theory of nonlinear fracture mechanics, which is associated with the crack opening law of a cohesive model.

For the material *model Concrete EC2-CC3DNonLinCementitious 2*, this law is given by the Hordijk [20] softening function presented in Figure 7a, where σ is the tensile stress, w is the crack opening, f_t^{ef} is the effective tensile stress and w_c is the crack opening value when σ=0. The compressive behavior of concrete is determined by a Hardening/ Softening Plasticity Model based on Menetrey-William [21] failure surface and is represented in ATENA by Fictitious Compression Plane Model [17]. The uniaxial stress-strain law has a linear descending branch, where the value of post-peak plastic displacement due to compression (w_d) is an input parameter. For normal concrete, the value of w_d is around 0,5 mm and it is used as a default for the definition of the softening in compression (Figure 7b).

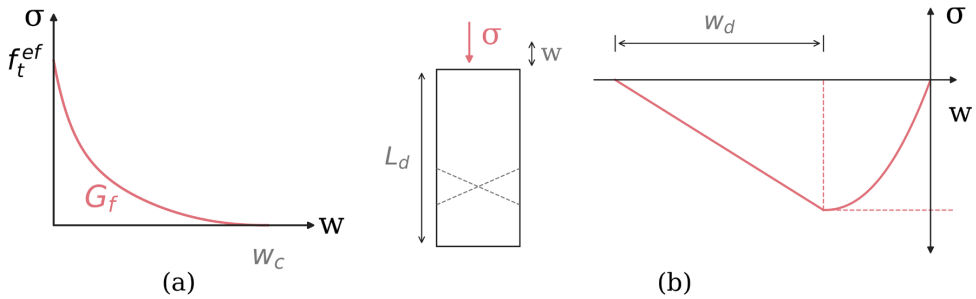


Figure 7. a) Plastic cohesive law with exponential softening in tension;
b) Compressive stress-strain diagram describing concrete behavior in compression.

The reinforcement was modeled using the material model *CCReinforcement*, which follows a stress–strain relationship based on the multilinear law. In the model, the last e_{ps} value defines the breaking strain for the reinforcement bar. It was used e_{ps2} as 0.005, f_1 as 560 MPa and f_2 as 588 MPa.

4.2 Numerical model parameters

The finite element used to represent concrete in the model was the quadratic finite element CHX60. The moisture value considered on the numerical model was 0,9728. The finite element used to represent the reinforcement in the model was the CCBarWithBond 3D.

Among the numerical methods provided by the ATENA program, the Newton-Raphson method was used to solve the nonlinear system, with line-search algorithm. The Newton-Raphson method is efficient for cases where the load values must be known and is often used for thermal load calculations. Four types of solution errors were used as verification: displacement increment; normalized residual force; absolute residual force; and dissipated energy. For the first three criteria, a value of 0.01 was adopted. For the dissipated energy, 0.0001 was adopted. The stopping criterion was in case the error exceeded the tolerance multiplied by the factor during the iterations (10000 for the first three criteria and 100000 for the last one), or at the end of the analysis step.

The mechanical parameters of plastic deformation of concrete (ε_{cp}) and the compressive strength at the beginning of the nonlinear behavior (f'_{c0}) were calculated according to the Equations 2 and 3:

$$\varepsilon_{cp} = \frac{f_{cm}}{E_{cm}} \tag{2}$$

$$f'_{c0} = 2 \cdot f_{tm} \tag{3}$$

The other parameters applied to the first model before final calibration (adjusted value) were used with the program's default values (initial value) and are shown in Table 3, where E_{cm}: elasticity modulus of concrete; ν: Poisson's ratio; f_{tm}: direct tensile strength; f_{cm}: cylindrical compressive strength; G_f : concrete fracture energy; s_F : shear factor; ε_{cp}: concrete plastic deformation; f'_{c0}: compressive strength of concrete at the beginning of the nonlinear regime; w_d : post-peak plastic displacement due to compression; $f_{c,red}$: reduction factor in the compressive strength of concrete; e: dimensionless eccentricity parameter; β: shear retention factor.

Table 3. Reference concrete parameters

Parameter			Initial value	Adjusted value	Observation
elasticity modulus of concrete	E_{cm}	[MPa]	38849.8	38849.8	
Poisson's ratio	ν	-	0.2	0.2	
direct tensile strength	f_{tm}	[MPa]	1.91	1.91	
tensile strength	f_{ct}	[MPa]	4.01	3.717	Based on Vieira [22]
cylindrical compressive strength	f_{cm}	[MPa]	34	34	
concrete fracture energy	G_f	[N/mm]	0.138	0.092	Model proposed by Vecchio and Collins [23]
embedded fissure model		-	fixed	fixed	
size of aggregate		[m]	0.02	0.01	
shear factor	s_F	-	1	50	
concrete plastic deformation	ε_{cp}	-	-0.0015636	-0.00172	Based on Smith [3]
compressive strength of concrete at the beginning of the nonlinear regime	f'_{c0}	[MPa]	4.01	4.01	
post-peak plastic displacement due to compression	w_d	[m]	-0.0005	-0.0005	
reduction factor in the compressive strength of concrete	$f_{c,red}$	-	0.8	0.8	
dimensionless eccentricity parameter	e	-	0.52	0.52	
shear retention factor	β	-	0	0	
tensile softening curve		-	Hordijk model	Hordijk model	
compression fracture energy	G_c	[N/mm]	13.8	9.2	Gc = 100*Gf [17]

4.3 Ambient temperature tests

This section presents the results of the unrestrained slab-column experiments, 100 mm with 0.8% steel (AU-100/0.8). The ultimate capacities of the ambient specimens were used to calculate the sustained load to be applied during the heated tests.

Calibration was performed to obtain a load–displacement curve that closely approximates the curve and the punching shear failure mode observed in the experimental test. The displacement considered was the one in the centre of the slab. The mesh model has the quadratic finite element CHX60, as analysed by Vieira *et al.* [22].

The calibration procedure was conducted in a structured manner to ensure a clear assessment of the influence of each parameter on the structural response. First, a mesh sensitivity analysis was performed to define an appropriate discretization. The mesh was progressively refined until the numerical results showed negligible variation, ensuring that the response was not affected by mesh dependency.

Second, the boundary conditions were calibrated through the adjustment of the vertical stiffness parameter (Kv) parameter, which represents the deformability of the experimental support system. The analysis was initiated with the default value of 37000 MPa, corresponding to an almost rigid support condition, and progressively reduced to 50 MPa. The range of values investigated is presented in Table 4. The value 100 MPa was selected, as it provided the best agreement with the experimental results, particularly in terms of displacement and overall load–deflection behavior.

Third, the material parameters were calibrated by varying the concrete elastic modulus (E) and the fracture energy (G_F) across different combinations. These parameters were chosen due to their direct influence on the initial stiffness, cracking behavior, and post-peak response of the slab. The tested combinations are summarized in Table 5.

The criterion adopted to evaluate the quality of the calibration was based on the agreement between experimental and numerical load x vertical displacement curves. Particular emphasis was placed on accurately reproducing the initial stiffness, the peak load, and the overall response curve throughout the loading history. The selection of the final parameter set was based on a global best-fit curve approach rather than a single-point comparison.

The calibration process can thus be summarized as: (1) mesh definition and verification; (2) calibration of the vertical stiffness parameter Kv; and (3) calibration of the material parameters E and G_F. The final set of parameters corresponds to the combination that yielded the closest overall agreement with the experimental behavior.

Using a fine mesh can improve the numerical response and reduce mesh-related inaccuracies. A mesh convergence study was performed through slab thickness to get a better load-deflection curve. The mesh started from 20 mm to 5 mm, uniformly divided. In order to better approximate the gradual heating of the slab, the mesh size used was varied through slab thickness (concentrated towards the heated surface). Through width and length (56 element layers), a 25 mm mesh was used, as in Figure 8. The selected mesh density is sufficient to accurately capture the structural response under fire exposure.

The displacement was measured using "monitor for point nearest IP – displacements" condition applied to the slab bottom surface, at the centre.

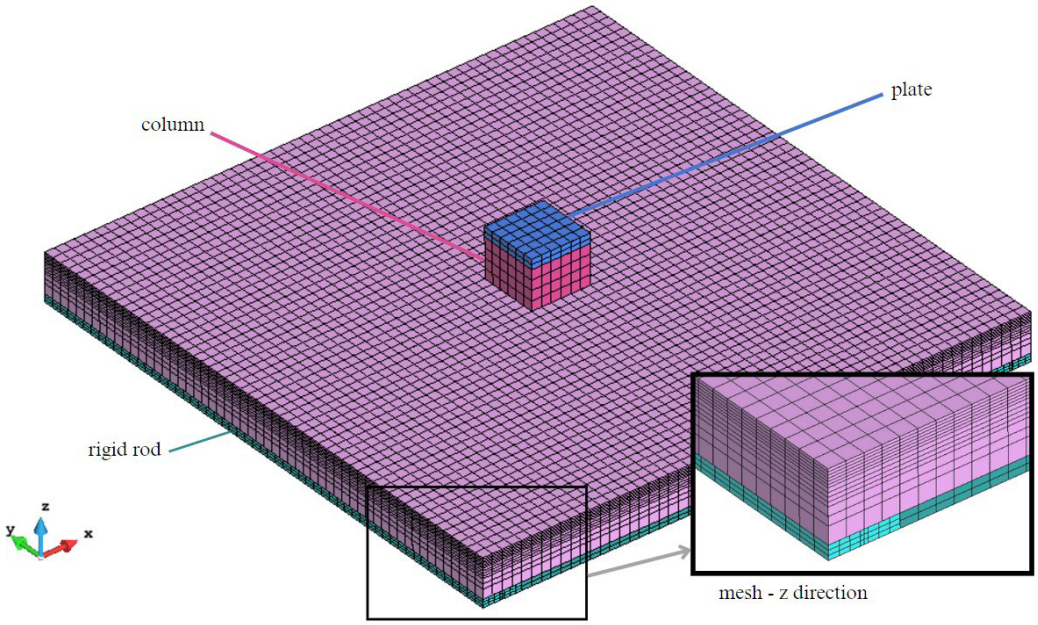


Figure 8. Finite element mesh adopted.

As boundary conditions, considering the slab as unrestrained (allowed to expand, and free to rotate), the slab rested on steel rods with spring criteria applied to the middle of bottom surface using the condition "spring for surface". Figure 9 shows the spring application.

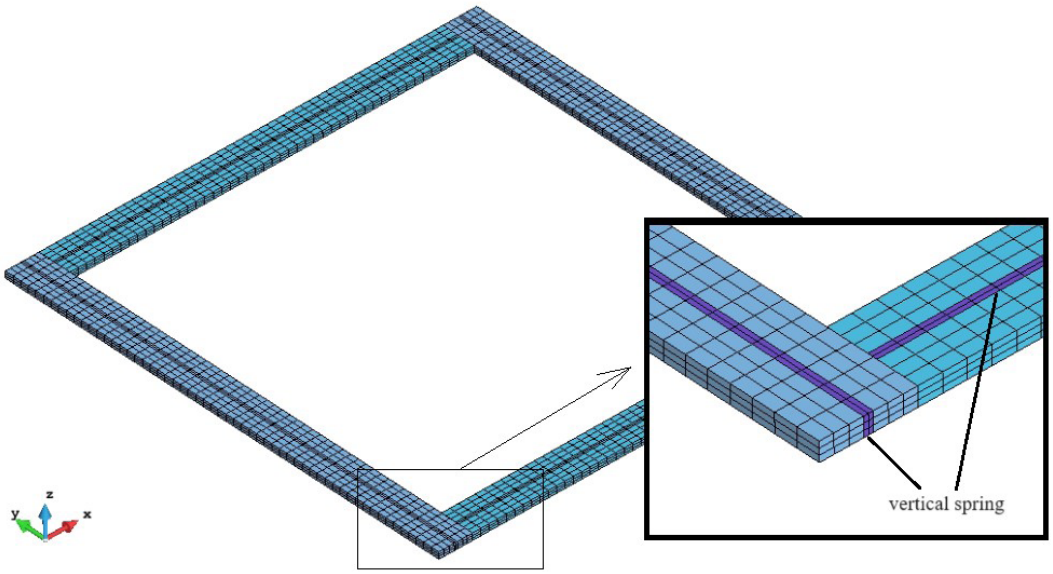


Figure 9. Vertical spring applied to bottom rods.

The influence of the spring stiffness is significant in flat slabs exposed to fire due to the interaction between thermal deformations and structural restraint. Fire induces temperature gradients that cause thermal expansion and curvature. When these deformations are restrained by the supports, additional internal forces and moments are generated. In flat slabs, this effect becomes critical. Moreover, the degradation of material properties at elevated temperatures reduces the slab's ability to redistribute stresses, increasing the importance of accurately representing support flexibility. A stiffer spring leads to higher restraint and internal forces, while a more flexible support allows greater deformation but reduces restraint-induced stresses.

4.4 Spring stiffness analysis

The vertical stiffness parameter (K_v) was calibrated through an iterative trial-and-error procedure to achieve the best agreement between the numerical predictions and the experimental results. From a physical standpoint, this parameter represents the overall deformability of the support system in the test setup, encompassing not only the stiffness of the bearing region but also local compliance effects associated with the contact interface, load transfer mechanisms, and possible micro-slips between the slab and its supports. Thus, K_v should be interpreted as an equivalent stiffness that captures the global boundary condition rather than a direct material property.

The analysis was initiated using the default stiffness value of 37000 MPa, which represents an almost rigid support condition, and was progressively reduced to as low as 50 MPa to capture the actual flexibility of the experimental setup. Table 4 summarizes the range of spring stiffness values investigated during this calibration process. The results indicate a strong influence of K_v on the structural response, particularly in terms of displacement and load distribution. The results indicate that lower values of K_v correspond to more flexible support conditions, leading to increased displacements and modified internal force distributions, whereas higher values tend toward a rigid-support assumption. The adopted value of 100 MPa provided the best correlation with the experimental results, particularly in terms of displacement response and overall structural behavior.

Table 4. Spring stiffness applied on the slab's supports

SPECIMEN ID	Kv (MPa)
AU-100/0.8-fixed	∞
AU-100/0.8-Kv-37000	37000 (default)
AU-100/0.8-Kv-18500	18500
AU-100/0.8-Kv-10000	10000
AU-100/0.8-Kv-5000	5000
AU-100/0.8-Kv-1000	1000
AU-100/0.8-Kv-500	500
AU-100/0.8-Kv-250	250
AU-100/0.8-Kv-100	100
AU-100/0.8-Kv-50	50

Figure 10 shows the load-deflection behaviour for spring calibration applied to unrestrained slab AU100-0.8, before heating.

It is possible to compare the experimental results (in red) with FE results, changing the vertical stiffness values. The difference between the experimental model and FE stiffness predictions is caused by the supporting reaction frame stiffness, which was not perfectly rigid. The discrepancy highlights the importance of the restraint conditions for FE modeling.

Additionally, the model designated as AU-100/0.8-fixed corresponds to a reference case without support rods, in which the slab is fully constrained in the vertical (Z) direction. This configuration represents an idealized boundary condition and serves as a benchmark for evaluating the effect of support flexibility in the calibrated models.

The vertical stiffnesses adopted for slab AU-100/0.8 was Kv = 100 MPa, as it was the one that gave the best approximation to the experimental model. Figure 11 shows the second step of FE calibration consisted of changing the concrete elastic modulus (E) and the fracture energy (G_F), for different combinations. The parameters are presented on Table 5.

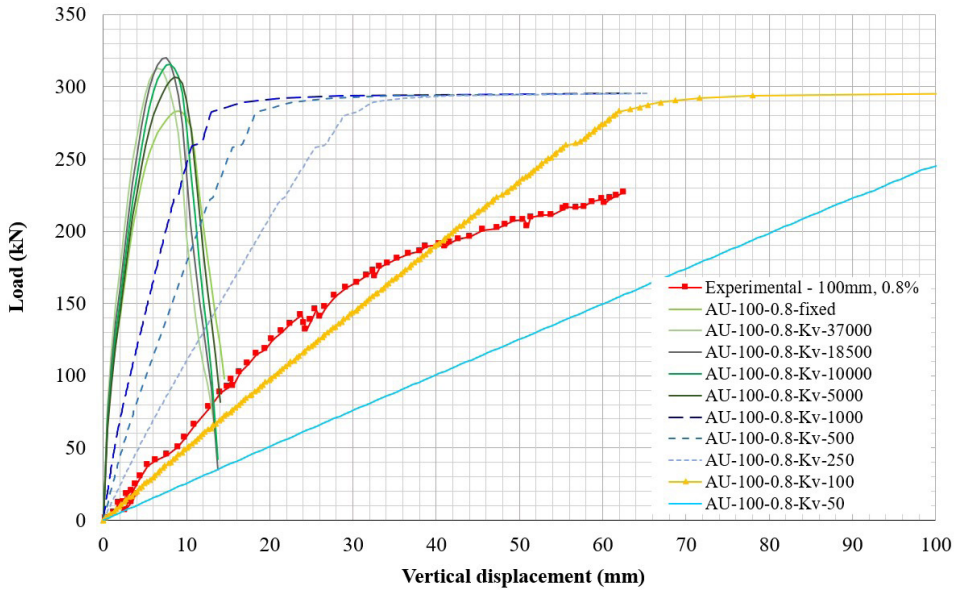


Figure 10. Spring calibration for load-deflection relations of slab AU100-0.8 at preloading phase in ambient temperature

Table 5. Concrete properties for calibration

SPECIMEN ID	E (MPa)	G_F (N/mm)
AU-100/0.8-Kv-100	38849.8	0.092
AU-100/0.8-Kv-100 – 2 GF	38849.8	0.276
AU-100/0.8-Kv-100 – 0.7 GF	38849.8	0.032
AU-100/0.8-Kv-100 – 0.5 GF	38849.8	0.046
AU-100/0.8-Kv-100 – 0.5 GF 0.5 E	19424.9	0.046
AU-100/0.8-Kv-100 – 0.5 E	19424.9	0.092
AU-100/0.8-Kv-100 – 0.1 GF 0.5 E	19424.9	0.014

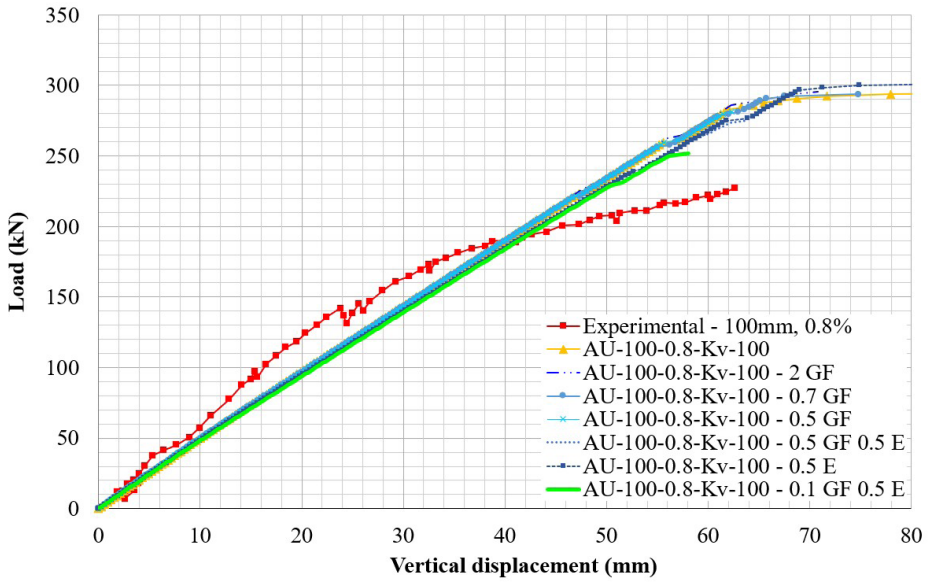


Figure 11. Concrete properties calibration for load-deflection relations of slab AU100-0.8 at the preloading phase in ambient temperature

The FE specimen which gave the best results was AU-100/0.8-Kv-100 – 0.1 GF 0.5 E.

4.5 Transport analysis

The moisture transport is given by the Equation 4:

$$\frac{w}{t} = \frac{\left(w_e + w_n\right)}{t} = -div\left(J_w\right) \tag{4}$$

where: w = total water content [mass/mass]; w_e , w_n = stands for the amounts of free and fixes water contents [mass/mass]; J_w = moisture flux [length·mass/time·mass]; t = time [time].

The moisture flux is given by Equation 5:

$$J_w = -D_w \cdot \nabla w_e \tag{5}$$

where: D_w = moisture diffusivity tensor of concrete [m²/day]; □ = gradient operator.

If usual Gauss integration and exact time derivatives are used, the solution may suffer from mass losses. Heat transfer is governed by Equation 6:

$$\frac{Q}{t} = \frac{\left(C_T\left(T - T_{ref}\right)\right.}{t} = C_T \frac{T}{t} = -div\left(J_w\right) \tag{6}$$

where: Q = total amount of energy [J/m³]; C_T = heat capacity [J/(K·m³)]; J_T = heat flux [J/(day·m²)].

Heat flux is given by Equation 7:

$$J_T = -K_T \cdot grad\left(T\right) \tag{7}$$

and K_T stands for heat conductivity [J/(day·m·K)].

Equation 7 accounts for heat transfer due to conduction only, and heat convection is negligible. However, it is not possible to neglect concrete moisture consumption due to the hydration process. Hydration water content w_h is given by Equation 8:

$$w_n = w_h \approx 0,21 \cdot c \cdot \left(\frac{t_e}{\tau_e + t_e}\right)^{1/3} \tag{8}$$

where: τ_e = 23 days; t_e = equivalent hydration time in water temperature 25°C.

ATENA has *CCTransport Material* as constitutive model available for transport analysis. Heat and moisture flow governing equations are given by:

Heat (Equation 9):

$$\frac{Q}{t} = C_{Th} \cdot \frac{h}{t} + C_{TT} \cdot \frac{T}{t} + C_{Tw} \cdot \frac{w}{t} + C_{Tt} = -\frac{}{t}\left(K_{Th} \cdot grad\ (h) + K_{TT} \cdot grad\left(T\right) + K_{Tw} \cdot grad\left(w\right) + K_{Tgrav}\right) \tag{9}$$

Moisture (Equation 10):

$$\frac{w}{t} = C_{wh} \cdot \frac{h}{t} + C_{wT} \cdot \frac{T}{t} + C_{ww} \cdot \frac{w}{t} + C_{wt} = -\frac{}{t}\left(D_{wh} \cdot grad\ (h) + D_{wT} \cdot grad\left(T\right) + D_{ww} \cdot grad\left(w\right) + D_{wgrav}\right) \tag{10}$$

Cervenka *et al.* [17] present all model definition and its expressions. The model assumes that concrete components consist of aggregate, filler, water and cement (Equation 11).

$$m_{concr} = m_{aggregate} + m_{filler} + m_{cement} + m_{water} \tag{11}$$

where m_{concr} is the mass of concrete per unit volume; $m_{aggregate}$ is the mass of aggregate; m_{filler} is the mass of filler; m_{cement} is the mass of cement; m_{water} is the mass of water.

The capacity of fresh cement paste yields (Equation 12):

$$C_{concr} = f_{aggregate} \cdot C_{aggregate} + f_{filler} \cdot C_{filler} + \hat{C}_{paste} \tag{12}$$

where C_{concr} is the concrete capacity. C_{paste} depends on the hydration degree α (Equation 13):

$$\hat{C}_{paste} = \left(f_{cement} \cdot C_{cement} + f_{water} \cdot C_{water}\right) \cdot \left(1 - 0.26 \cdot \left(1 - exp\left(-2.9 \cdot \alpha\right)\right)\right) \quad (13)$$

where C_{cement} is the cement capacity at time zero.

According to Cervenka *et al.* [17], the heat capacity of structural concrete is between 0.8 and 1.17 J/(kg·K). $C_{aggregate}$ is 840 J/(kg·K) for basalt and limestone,790 J/(kg·K) for granite, and 800 J/(kg·K) for sand. C_{cement} is approximately 750 J/(kg·K) and C_{water} is 4180 J/(kg·K).

4.5.1 Concrete properties for transport analysis

Concrete was modeled using *CCTransport Material* as constitutive model, with the properties shown in Table 6. The initial values are the ATENA default parameters available. The adjusted values presented in Table 6 are the values used on the numerical model, according to the experimental data.

Table 6. Concrete parameters for transport analysis

Parameter			Initial value	Adjusted value	Observation
thermal conductivity	K_{temp}	[W/(°Cm)]	2.1	1.1	
thermal capacitance	C_{temp}	[kN/(m²°C)]	2550	2550	
initial temperature		[°C]	25	22	Based on [3]
moisture		[-]	0.9728	0.96	Based on [3]
emissivity	ε	[-]	-	0.70	Based on [5]
type of conductivity			lower limit		

The emissivity (ε) value for the radiation process was defined based on EN 1992-1-2:2023 [5]. Analyses were done using different values of ε and results show that ε = 0.7 could produce a good comparison of temperature profile with the test results.

5 CRACK OPENING NUMERICAL ANALYSIS

A numerical analysis of the crack opening was conducted to understand the differences between heated and ambient temperature models. The equations were solved using Newton-Raphson method. The iteration limit was defined as 150. The meshed model consisted of 52107 nodes. The hydraulic loading of 25000 kN/m² was applied using the condition “displacement for surface”, directly to the 25 mm thick steel loading plate, which distributed the load to the 120x120 mm column stub surface. It was distributed in 200 load steps.

5.1 Numerical analysis – ambient temperature

The final properties adopted after calibration are presented on Table 7.

5.1.1 Crack pattern

Figure 12 shows the failure cross-sectional crack patterns of the AU-100/0.8 slab. The direction, N–S of the frame, depicts which cross-sectional half is presented. The blue arrows indicate the reaction forces acting on the slabs, whereas the load applied is shown with black arrows. Figure 13 also shows the failure cross-sectional crack patterns of the AU-100/0.8-Kv-100 – 0.1 GF 0.5 E finite element slab, obtained from ATENA analysis. Clipping plane: (1.4, 0.7, -0.1)x(1.4, 0.7, 0.0)x(0.0, 0.7, -0.1).

The red marks in Figure 13 shows the crack pattern on the slab surface for experimental model by Smith [3] and the failure crack patterns of the AU-100/0.8-Kv-100 – 0.1 GF 0.5 E finite element slab surface (top and bottom), obtained from ATENA analysis.

Table 7. Concrete parameters after calibration

Parameter			Calibrated value
elasticity modulus of concrete	E_{cm}	[MPa]	19424.9
Poisson's ratio	ν	-	0.2
direct tensile strength	f_{tm}	[MPa]	1.91
tensile strength	f_{ct}	[MPa]	4.01
cylindrical compressive strength	f_{cm}	[MPa]	34
concrete fracture energy	G_f	[N/mm]	0.0137
embedded fissure model		-	fixed
size of aggregate		[m]	0.01
shear factor	s_F	-	50
concrete plastic deformation	ε_{cp}	-	-0.001750
compressive strength of concrete at the beginning of the nonlinear regime	f'_{c0}	[MPa]	4.01
post-peak plastic displacement due to compression	w_d	[m]	-0.0005
reduction factor in the compressive strength of concrete	$f_{c,red}$	-	0.8
dimensionless eccentricity parameter	E	-	0.52
shear retention factor	β	-	0
tensile softening curve		-	Hordijk model
compression fracture energy	G_c	[N/mm]	13.7

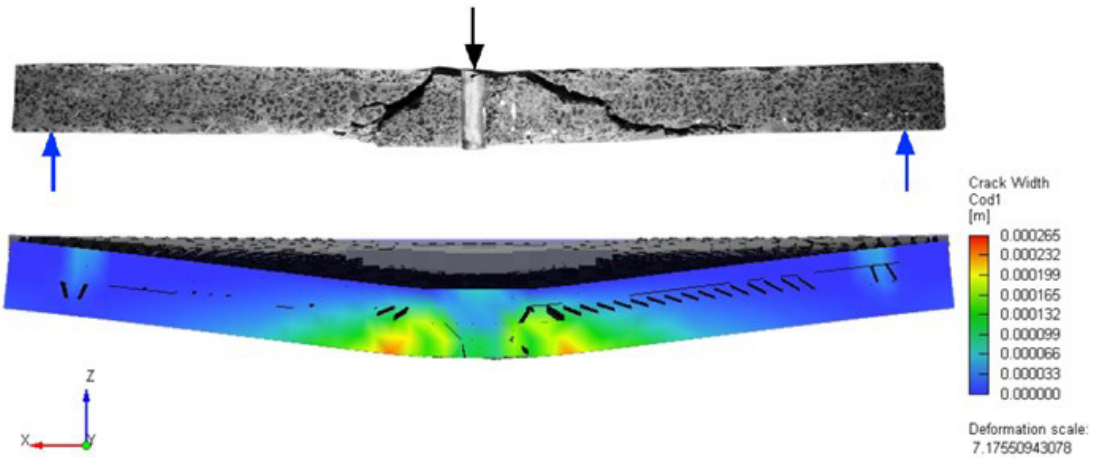


Figure 12. Cross-sections of AU-100/0.8 and AU-100/0.8-Kv-100 FE slab showing the post-failure crack patterns (Smith [3]) and FE slab.

The cracks observed on the bottom surface align with the flexural reinforcement.

5.2 Numerical analysis – heated

This section presents the results of the heated unrestrained slab-column experiments, 100 mm with 0.8% steel (HU100-0.8). The thermal field from a natural fire is not as severe as a standard fire, as presented by Bamonte *et al.* [2]. 45 minutes ISO-834 fire duration is like 100 minutes of natural fire. It is essential to analyse the indirect actions caused by natural fires accurately using a standard fire to assess structural behaviour, as BS EN 1992-1-2:2023 [5] often underestimates them.

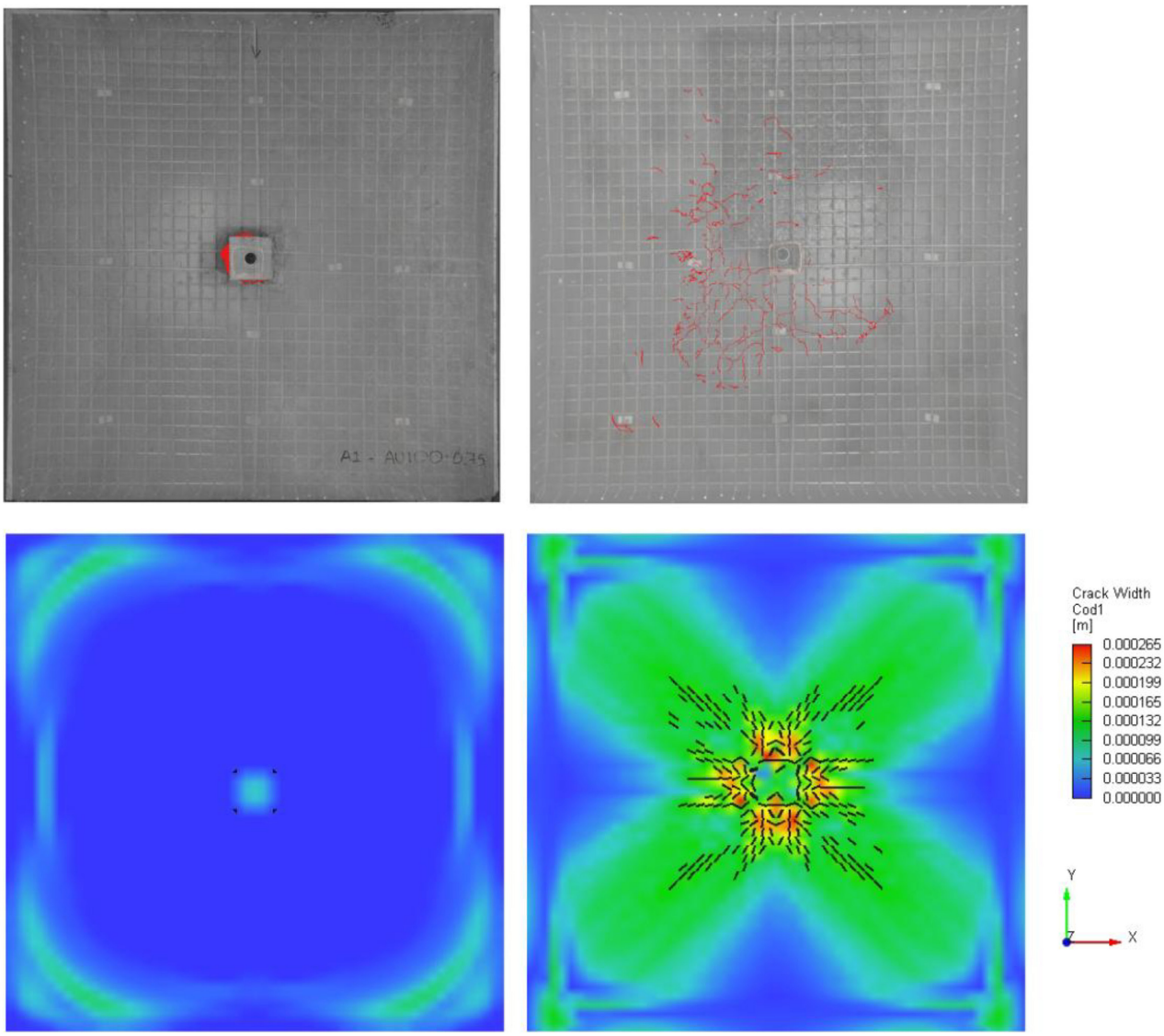


Figure 13. Ambient 100 mm thick, 0.8% reinforced: unrestrained slab showing the plan post-failure crack patterns. Left: top surface. Right: bottom surface (Smith [3]) and FE slab.

The load applied to the heated specimen was factored by taking Muttoni's CSCT (Critical Shear Crack Theory) [2] predictions into consideration and is presented in Table 8. The experimental failure load was compared with the predicted resistance, and the percentage difference was calculated using Equation (14). This difference was then used to adjust the predicted failure load according to Equation (15). The applied load for the heated test was taken as 70% of the ambient capacity, as expressed in Equation (16), considering the provisions of BS EN 1992-1-2:2023 [5]. The slabs were loaded at a displacement rate of 2 mm/min (numerical load). Table 8 compares the Muttoni-designed failure loads with the experimentally measured values.

Table 8. Ambient experimental failure load and calculated applied load for heated test

SPECIMEN ID	Experimental failure load (kN)	Muttoni Design Failure Load (kN)	Failure load difference (kN)	Factored Muttoni design load (kN)	Applied load for heated test (kN)
AU-100/0.8	226.3	144	57.2	242	174.6

where:

$$\text{failure load difference} = 100 \cdot \frac{\left(\text{experimental failure load} - \text{Muttoni design failure load}\right)}{\text{Muttoni design failure load}} \tag{14}$$

$$\text{factored Muttoni design load} = \text{Muttoni design failure load} \cdot \left(1 + \frac{\left(\text{failure load difference}\right)}{100}\right) \tag{15}$$

$$\text{applied load for heated test} = 0,7 \cdot \text{Factored Muttoni design load} \tag{16}$$

Table 9 presents the failure load and corresponding displacement. The slabs had a moisture content of 4%. The steel reinforcement is the same as for the ambient temperature tests. Smith [3] highlighted the following points: the slab failed 4 minutes after ignition; the maximum approximate concrete temperature near the heated surface was 130°C; the flexural steel at an adequate depth of 81mm reached 18°C.

Table 9. Data for AU-100/0.8 and HU-100/0.8 models

SPECIMEN ID	Load applied during heating (kN)	Failure load (kN)	Displacement at failure load (mm)
AU-100/0.8	-	226.3	62.4
HU-100/0.8	174.6	174.8	30.8

5.3 NLFE Transport Analysis

The NLFE analysis aimed to replicate the temperatures within the slabs that were measured by thermocouples during the tests [3]. The thermal flux of 40000 W/m^2 was applied as *Neumann temperature for surface* on the upper surface (compression). The slab was loaded prior the heating, and it was sustained during the heated test. The applied load is presented in Table 9. As the NLFE analysis did not model moisture movement explicitly, discrepancy is expected. The effects of moisture were included through the variation in the concrete specific heat with temperature. To allow the heat to be applied after initial load, 2 interval data were created. Interval data 1: 100 load-steps, ambient temperature; Interval data 2: 100 load-steps, heated.

5.3.1 Displacement measurement

The slab was stiffer during the load phase compared to the ambient tested slab. Smith [3] conducted the heated test with 77% of the failure load for ambient temperature. For this load, the NLFE model predicts a high deflection after a short duration of heating. In the thermal model, initial thermal properties were computed, and nodal temperatures were generated. Figure 14 shows the temperature contours for the thermal analysis.

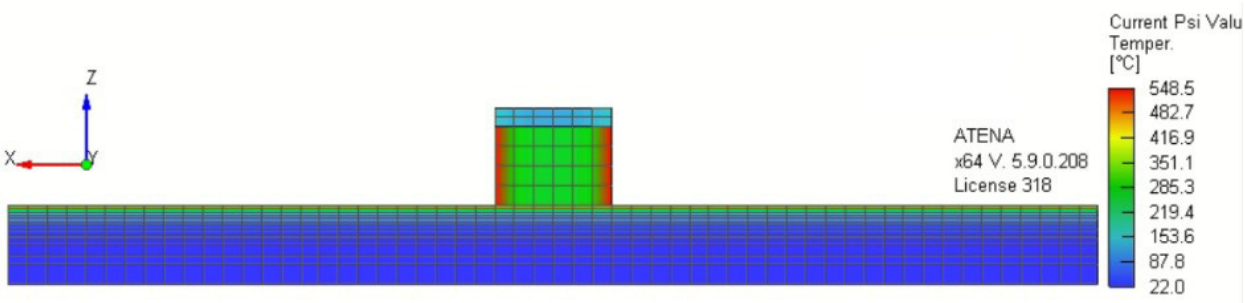


Figure 14. Temperature contours in the slab cross section for thermal results at time 600s.

For the thermomechanical model, the thermal model data (from step) were imported into the static model. Figure 15 presents the load-displacement curve for both experimental and numerical model.

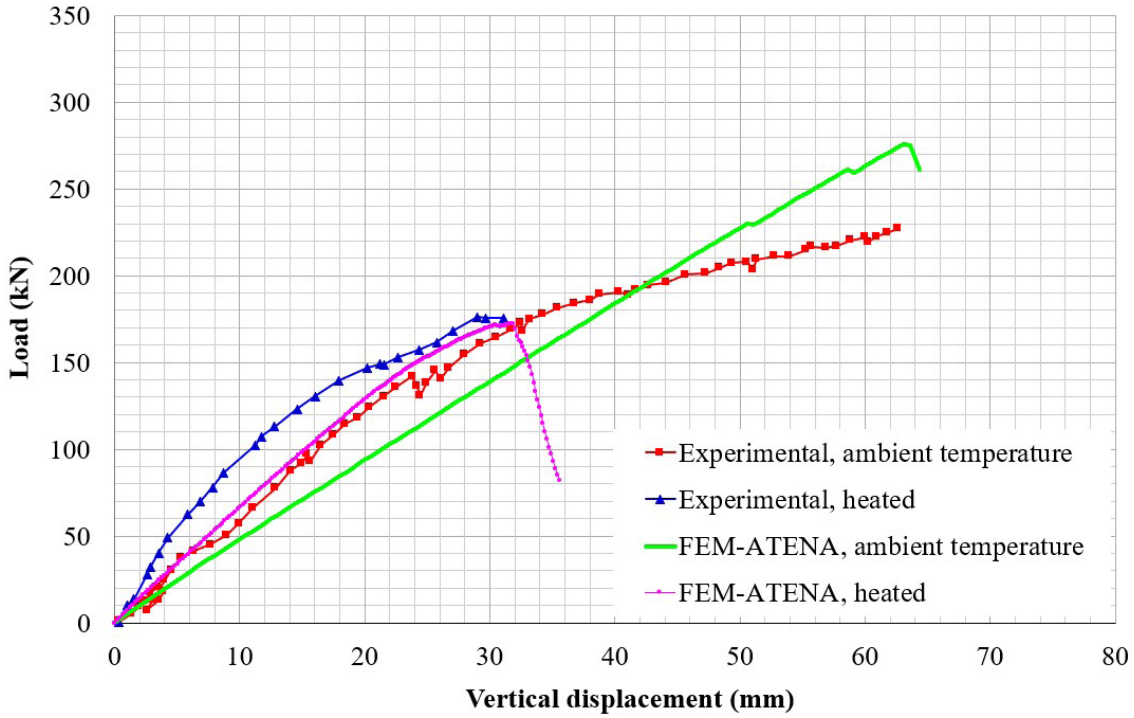


Figure 15. Load-deflection behaviour of HU-100/0.8 model.

5.3.2 Failure crack pattern

Figure 16 shows the failure cross-sectional crack patterns of the HU-100/0.8 slab and the finite element slab, obtained from ATENA analysis. Clipping plane: (1.4, 0.7, -0.1)x(1.4, 0.7, 0.0)x(0.0, 0.7, -0.1). The direction, N–S of the frame, depicts which cross-sectional half is presented. The blue arrows indicate the reaction forces acting on the slabs. The load applied is shown with black arrows.

The cracks observed on the top surface in Figure 17 emanate around the loaded column stub.

Figure 17 demonstrates that the heat exposure increases the reinforcement stress beyond the yield stress, in agreement with the findings of [24]–[26]. As a result, the failure pattern is no longer brittle punching.

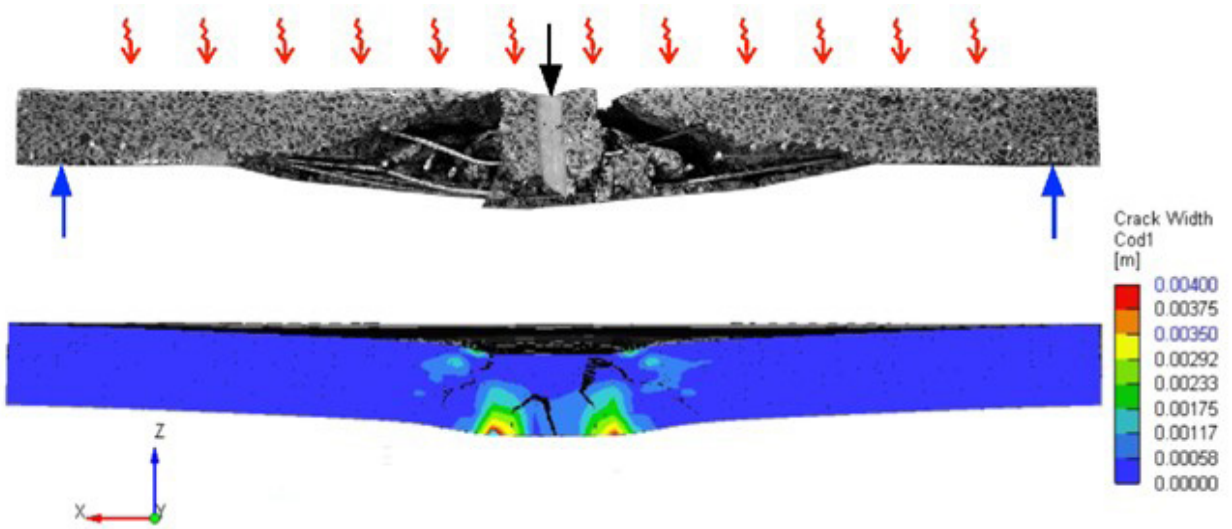


Figure 16. Cross-sections of HU-100/0.8 slab with the post-failure crack patterns – applied load 174.6 kN (Smith [3]) and FE slab.

6 DISPLACEMENT RATE ANALYSIS

From the calibrated model, a parametric analysis was carried out to understand the effects of load levels for the crack opening.

The load rate was not varied to represent experimental conditions, but as a numerical strategy associated with the displacement-controlled analysis adopted to capture the full structural response, including the post-peak behaviour. In this study, the objective was not to reproduce the exact loading rate of the experimental tests, but to evaluate the ultimate capacity and failure mechanism of the slab.

Figure 18 shows the load-displacement curves for different load levels. The calibration model was loaded using the condition "displacement for surface" of 0.2mm/min. It was distributed in 200 load steps.

It can be noted that increasing the load rate, the maximum temperature at failure decreases, indicating that higher load rates decrease the slab resistance.

A significant discrepancy was observed between the experimentally measured temperature (approximately 130 °C) and the value predicted by the numerical model (323.6 °C). This difference can be primarily attributed to uncertainties and limitations inherent to temperature measurements during the experimental test. In particular, thermocouple readings are highly sensitive to their exact positioning within the slab, the quality of thermal contact with the surrounding material, and the sensor's thermal inertia. These factors may lead to an underestimation of the actual temperature within the structural element. Furthermore, local material heterogeneities and possible shielding effects within the specimen may have influenced the recorded temperatures. In the experimental model, the temperature was recorded using 3 trees with 5 thermocouples each through the slab depth. Figure 20 presents the thermocouple depths from the heated surface of the slab and the position of the 3 thermocouple trees.

In contrast, the numerical model computes the temperature field under idealized conditions, assuming homogeneous material properties and prescribed boundary conditions. The latter include uniform thermal exposure, as well as simplified representations of convective and radiative heat transfer, which may contribute to higher predicted temperatures. Moreover, small deviations between the exact thermocouple positions and the corresponding locations extracted from the numerical model may contribute to differences in temperature values, particularly in regions with steep thermal gradients. Although the numerical model overestimates the absolute temperature values relative to the experimental measurements, this outcome can be considered conservative from a structural analysis perspective, as higher temperatures generally result in a greater degradation of mechanical properties. Importantly, the model is able to reproduce the overall thermal evolution observed experimentally. Therefore, while the observed discrepancy underscores the inherent uncertainties associated with experimental temperature measurements, it does not compromise the validity or robustness of the proposed thermo-mechanical modelling approach.

Figure 19 presents the temperature contour for the thermomechanical models. Figure 19-a represents the HU-100/0.8 slab loaded of 1.0 mm/min. Figure 19-b represents the HU-100/0.8 slab loaded of 0.6 mm/min. Figure 19-c represents the HU-100/0.8 slab loaded of 0.2mm/min.

During the exposition to fire, the concrete cracking occurs due to the tensile strength exceeding, caused by thermal expansion and dehydration. When concrete surface cracking happens, pathways for direct reinforcement bars heating can occur, bringing more thermal stress. The crack width is calculated by multiplying the crack spacing by the crack inducing strain. Analysing the models, the slab loaded at 1.0 mm/min presented 3.19 mm-cracks right before failure, while the slab loaded at 0.6 mm/min presented 2.81 mm-cracks right before failure, and the slab loaded at 0.2 mm/min presented 1.85 mm-cracks right before failure. Figure 21 presents the crack width for the thermomechanical models.

Figure 21-a represents the HU-100/0.8 slab loaded of 1.0 mm/min. Figure 21-b represents the HU-100/0.8 slab loaded of 0.6 mm/min. Figure 21-c represents the HU-100/0.8 slab loaded of 0.2 mm/min.

Although the analysis of crack opening gives important information about the local behavior around the slab–column connection, the load–deflection curves show that the investigated parameters also affect the global response of the slab. As the temperature increases, a clear reduction in stiffness can be observed, with a softer slope in the curves, together with a decrease in the ultimate load. This is mainly related to the degradation of the concrete properties at high temperatures and the increase in cracking.

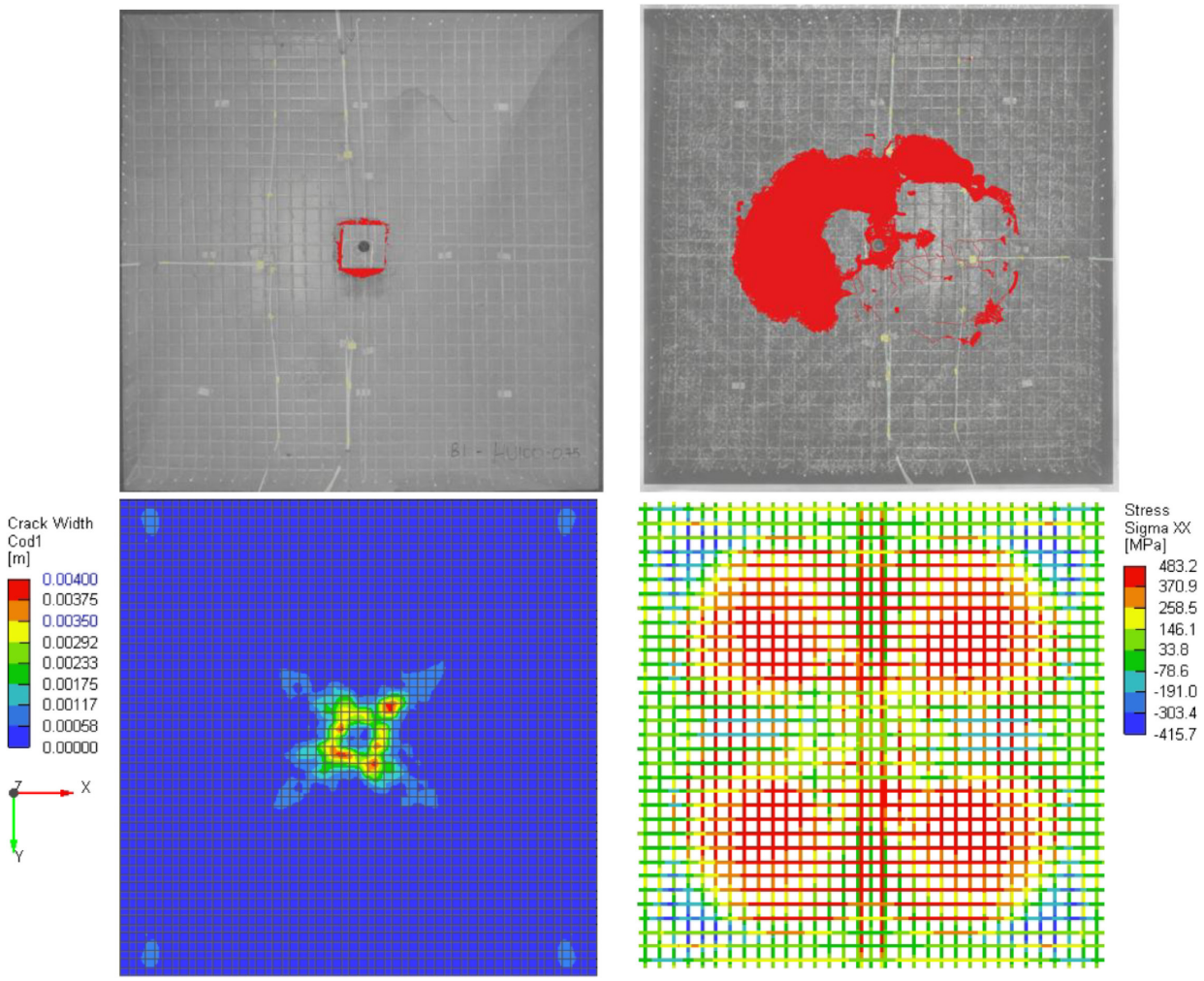


Figure 17. Heated 100 mm thick, 0.8% reinforced: unrestrained slab showing the plan post-failure crack patterns. Left: top surface. Right: bottom surface (Smith [3] and FE model).

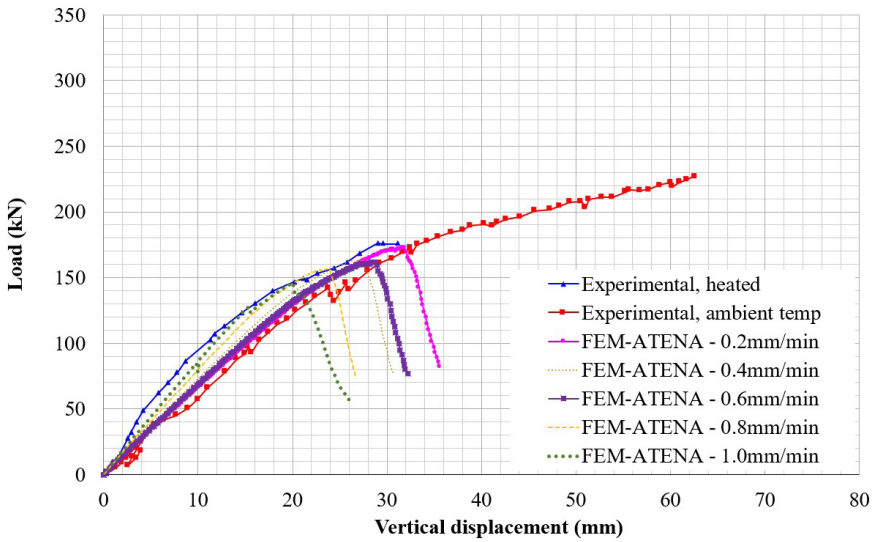


Figure 18. Load-displacement curve for HU-100-0.8 slab.

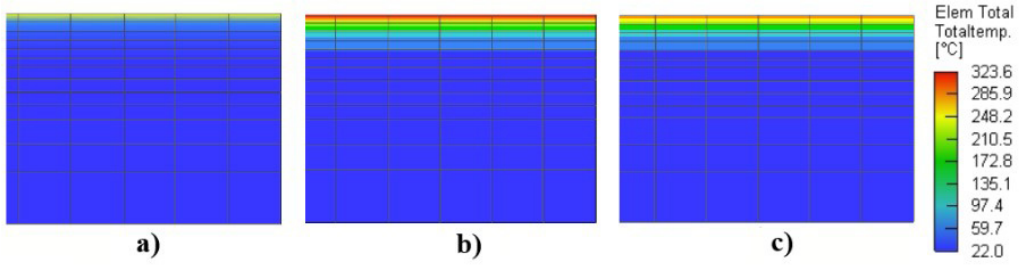


Figure 19. Temperature contours in the slab cross section for thermomechanical results at failure. Loads: a) 1.0 mm/min, b) 0.6 mm/min, c) 0.2 mm/min.

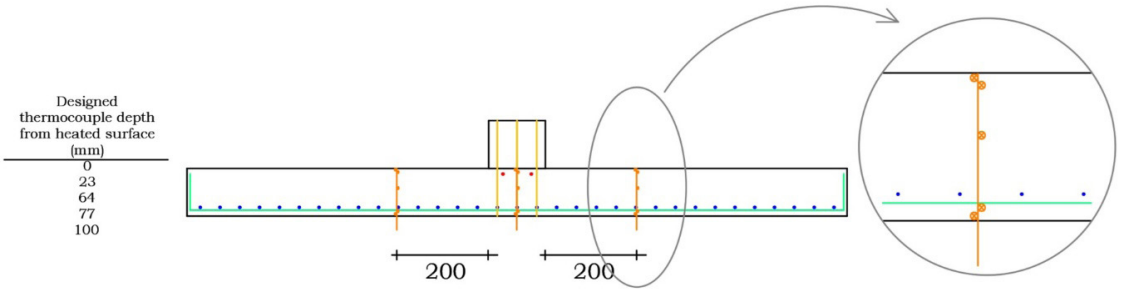


Figure 20. Thermocouples position in the slab (units in mm)

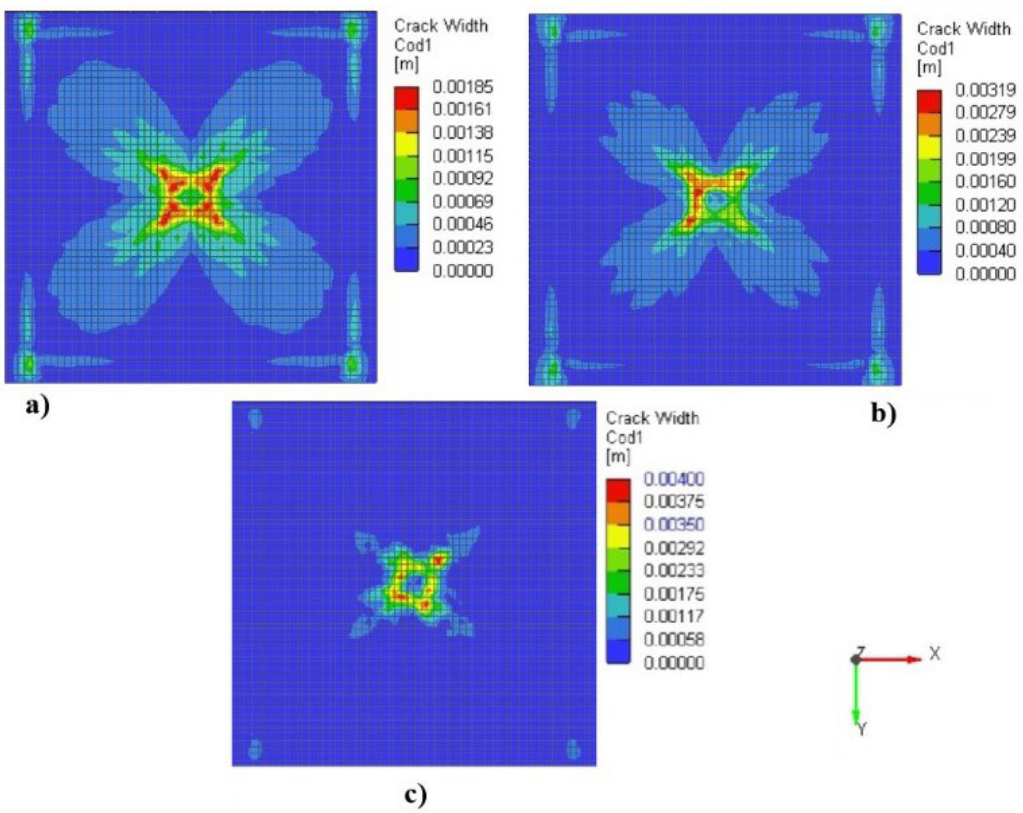


Figure 21. Crack width for thermomechanical results at failure. Loads: a) 1.0mm/min, b) 0.6mm/min, c) 0.2mm/min.

Increasing the load level before fire exposure leads to higher initial damage and reduces the deformation capacity of the slab, resulting in earlier punching failure and lower residual strength. Although crack opening increases significantly with temperature, it does not always follow the same pattern as the reduction in ultimate capacity. Overall, the results indicate that the behavior is governed by the interaction between cracking, stiffness degradation, and load level, especially in the slab–column region where punching occurs. Therefore, crack opening alone is not sufficient to describe the structural response under fire conditions. It is also necessary to consider the load–deflection behavior and the ultimate capacity to better understand the failure mechanism and the overall performance of the slab.

7 CONCLUSIONS

The finite element (FE) analysis indicates that, under the applied load, the slab exhibits a rapid and unstable increase in deflection shortly after the onset of heating. This behavior arises from the accelerated development of plastic strain, as reflected in the evolution of the maximum principal plastic strain shortly after thermal exposure. The results suggest that early tensile crack initiation plays a significant role in promoting this rapid deflection growth, highlighting the sensitivity of the structural response to thermally induced degradation mechanisms. These findings underscore the importance of accurately capturing material nonlinearity and cracking behavior in fire-exposed structural analyses to ensure reliable predictions of load-bearing capacity and structural integrity during fire events.

The numerical models analysed in this study aimed to understand the effect of the load on the crack opening of flat slabs under heat conditions for which there are few studies. It is important to note that the heat applied to the top surface corresponds to bottom surfaces exposure in real life. No shear reinforcement was considered as it has small effect on the fire resistance of a slab, as presented by the literature.

The load levels were the parametric focus. The findings of this study are as follows.

- The spring calibration conducted allowed to compare the experimental results from Smith [3] with FE results, changing the vertical stiffness values. The difference between the experimental model and FE stiffness predictions is caused by the supporting reaction frame stiffness, which was not perfectly rigid. The discrepancy highlights the importance of the restraint conditions for FE modeling.
- During calibration, the ATENA model was loaded at 0.2 mm/min rate distributed in 200 load steps. The load rate affects the slab displacement and fire resistance of the slab. The slab experimentally tested by Smith [3] was loaded by the same 0.2mm/min rate, and it failed in catastrophic punching shear.
- The ATENA model reached a maximum temperature of 323.6 °C. The maximum temperature that the slab experimentally tested by Smith [3] reached was 130 °C. The difference can be due to the measurement equipment applied.
- Analysis of the models revealed that the slab loaded at 1.0 mm/min developed 3.19 mm cracks just before failure, compared with 2.81 mm for the slab loaded at 0.6 mm/min and 1.85 mm for the slab loaded at 0.2 mm/min. These findings demonstrate that the displacement rate directly affects the cracking behaviour of flat slabs exposed to fire.
- Higher displacement rates produced larger crack widths before failure, reflecting a more brittle structural response, whereas lower rates resulted in smaller cracks and a more gradual progression toward collapse. These outcomes emphasize the importance of accurately calibrating spring stiffness and carefully selecting loading parameters in numerical models, as both significantly affect the predicted structural response under fire conditions.
- The main contribution of the parametric analysis was to fill a niche gap in the understanding of load influence on the crack opening of flat slabs in fire, as different load rate analyses with a full description of the parameters are not frequently presented in the literature.
- With the definition of the cracking pattern for each of the different load rate, the basis for the future development of a model for predetermining the spalling behaviour of slabs exposed to fire can be provided.
- In real fire scenarios, the mechanical load is typically applied prior to the fire event and remains essentially constant during heating. Therefore, the variation in loading rate adopted in this study does not aim to directly replicate actual construction conditions. Instead, the use of different loading rates is primarily intended to support the calibration and verification of the numerical model. It allows for the assessment of the model's sensitivity to the interaction between mechanical loading and thermal effects, as well as ensuring numerical stability and convergence throughout the analysis. While the loading rate variation does not represent a

realistic fire scenario, it constitutes a methodological tool that contributes to the robustness, reliability, and calibration of the proposed numerical model.

The results highlight the importance of accurately representing boundary conditions in the analysis of flat slabs under fire. In particular, the flexibility of the supports was shown to significantly influence the structural response, especially in terms of displacement and load redistribution. Therefore, assuming fully rigid supports may lead to unconservative or unrealistic predictions. Engineers should consider adopting equivalent support stiffness values that reflect the actual restraint conditions of the structure. Additionally, the rate of loading and the sequence of thermo-mechanical actions play a relevant role in the response, indicating that simplified approaches that neglect these aspects may overlook critical behaviors during fire exposure.

About limitations, the study is based on a single slab geometry without shear reinforcement, which restricts the direct applicability of the results to other configurations. The analysis also considers a single concrete type. These simplifications may influence the predicted temperature field and, consequently, the structural response under fire conditions.

Regarding generalizability, while the adopted modelling approach and calibration procedure can be extended to other slab geometries and fire conditions, the specific numerical results should be interpreted with caution. The sensitivity of the response to parameters such as support stiffness, material properties, and thermal boundary conditions suggests that similar analyses should be conducted for different structural configurations to ensure reliable predictions. Future studies should therefore investigate a broader range of slab geometries, reinforcement layouts, and fire exposure scenarios to validate and expand the applicability of the proposed study.

ACKNOWLEDGEMENTS

The authors greatly appreciate the financial support provided by Coordenação de Aperfeiçoamento de Pessoal de Nível Superior (CAPES).

REFERENCES

[1] R. A. S. Días, "*Análise numérica da resistência à punção de lajes lisas protendidas com cabos não aderentes*," M.S. thesis, Univ. Est. Campinas, Campinas, Brazil, 2018, https://doi.org/10.47749/T/UNICAMP.2018.1060215.

[2] P. Bamonte, R. Felicetti, and P. G. Gambarova, "Punching shear in fire-damaged reinforced concrete slabs,", *ACI Special Publication 265 "Thomas T.C. Hsu Symposium on Shear Torsion Concr. Struct."*, vol. 6, no. 265, pp. 345–366, 2009.

[3] H. K. Smith, "*Punching shear of flat reinforced-concrete slabs under fire conditions*," Ph.D. dissertation, The Univ. Edinburgh, 422 p., 2016. [Online]. Available: https://era.ed.ac.uk/handle/1842/20962?show=full

[4] C. N. Costa, "*Dimensionamento de elementos de concreto armado em situação de incêndio*," Ph.D. dissertation, Univ. São Paulo, São Paulo, Brazil, 2008, https://doi.org/10.11606/T.3.2008.tde-04092008-155911.

[5] European Standard, *Eurocode 2 - Design of Concrete Structures. Part 1-2: General Rules — Structural Fire Design*, EN 1992-1-2, 2023.

[6] Y. Anderberg and S. Thelandersson, *Stress and Deformation Characteristics of Concrete at High Temperatures 2. Experimental Investigation and Material Behaviour Model* (Bulletin of Division of Structural Mechanics and Concrete Construction 54). Lund: Lund Institute of Technology, 86 p., 1976.

[7] A. R. Fanton, "*Análise numérica do comportamento termomecânico de lajes de concreto armado expostas ao fogo*," M.S. thesis, Univ. Est. Campinas, Campinas, Brazil, 2019, https://doi.org/10.47749/T/UNICAMP.2019.1101303.

[8] D. P. Maximiano, "*Análise numérica avançada de estruturas de aço e de concreto armado em situação de incêndio*," Ph.D. dissertation, Univ. Fed. Ouro Preto, Ouro Preto, Brazil, 2018. [Online]. Available: https://www.repositorio.ufop.br/bitstream/123456789/10033/1/TESE_An%C3%A1liseNum%C3%A9ricaAvan%C3%A7ada.pdf

[9] H. Sadaghian and M. Farzam, "Numerical investigation on punching shear of RC slabs exposed to fire," *Comput. Concr.*, vol. 23, no. 3, pp. 217–233, 2019, https://doi.org/10.12989/cac.2019.23.3.217.

[10] I. Fletcher *et al*., "Performance of concrete in fire: a review of the state of the art, with a case study of the windsor tower fire," in *Proc. 4th Int. Workshop - Structures in Fire*, Aveiro, Portugal, 2006, pp. 779–790.

[11] Westergaard H., "Bearing pressures and cracks," *J. App. Mech.*, vol. 6, 1937.

[12] H. M. Sadd, *Elasticity: Theory, Applications and Numerics*, 4th ed. Oxford, England: Academic Press, 624 p., 2020.

[13] A. R. Fanton *et al*., "Numerical analysis on the load influence for the crack opening on flat slabs exposed to fire," in *Proc. IFireSS 2025 – 5th Int. Fire Saf. Symp. - Ulster University*, Belfast, 2025.

[14] E. Annerel, L. Taerwe, B. Merci, D. Jansen, P. Bamonte, and R. Felicetti, "Thermo-mechanical analysis of an underground car park structure exposed to fire," *Fire Saf. J.*, vol. 57, pp. 96–106, 2013, https://doi.org/10.1016/j.firesaf.2012.07.006.

[15] S. Guandalini, O. Burdet, and A. Muttoni, "Punching tests of slabs with low reinforcement ratios," *ACI Struct. J.*, vol. 106, no. 10, pp. 87–95, 2009.

[16] European Standard, *Eurocode 2 - Design of Concrete Structures – Part 1-1: General Rules and Rules for Buildings*, EN 1992-1-1, 2023.

[17] V. Cervenka, L. Jendele, and J. Cervenka, *ATENA Program Documentation, Part 1: Theory*. Prague: Cervenka Consult., 2017.

[18] Y. R. Rashid, "Ultimate strength analysis of prestressed concrete pressure vessels," *Nucl. Eng. Des.*, vol. 7, no. 4, pp. 334–344, 1968, https://doi.org/10.1016/0029-5493(68)90066-6.

[19] Z. P. Bažant and B. H. Oh, "Crack band theory for fracture of concrete," *Mater. Constr.*, vol. 16, no. 3, pp. 155–177, 1983, https://doi.org/10.1007/BF02486267.

[20] D. Hordijk, "*Local approach to fatigue of concrete*," Ph.D. dissertation, Delft Univ. Technol., Delft, The Netherlands, 1991.

[21] P. Menetrey and K. J. William, "Triaxial failure criterion for concrete and its generalization," *ACI Struct. J.*, vol. 36, no. 3, pp. 311–318, 1995, https://doi.org/10.14359/1132.

[22] P. H. S. M. Vieira, R. S. Díaz, M. G. Marques, E. A. P. Liberati, and L. M. Trautwein, "Nonlinear analysis of the impact of openings on punching shear strength," *Struct. Concr.*, vol. 24, no. 6, pp. 7334–7354, 2023, https://doi.org/10.1002/suco.202300476.

[23] F. J. Vecchio and M. P. Collins, "The modified compression-field theory for reinforced concrete elements subjected to shear," *ACI Struct. J.*, vol. 83, no. 2, pp. 219–231, 1986.

[24] H. Sadaghian, S. S. Mirrezaei and M. Farzam, "Numerical simulation of punching shear in RC slabs subjected to elevated temperatures," *Mag. Concr. Res.*, vol. 76, no. 1, pp. 1–19, 2023, https://doi.org/10.1680/jmacr.22.00350.

[25] A. R. Fanton, L. C. Almeida, and L. M. Trautwein, "Parametric analysis of thermo-mechanical behavior of reinforced concrete slabs with different aggregates in fire," *Rev. IBRACON Estrut. Mater.*, vol. 17, no. 5, pp. e17507, 2024, https://doi.org/10.1590/s1983-41952024000500007.

[26] A. R. Fanton *et al*., "Load-deflection behaviour of flat slab exposed to fire: parametric analysis on the spring stiffness influence," in *Proc. III SBPEC – Simp. Bras. sobre Punção em Estr. de Concreto – University of Campinas*, Campinas, 2025.

Author contributions: ARF: investigation, data curation, writing – original draft. LCA: supervision, project administration, funding acquisition, writing - review & editing. LMT: supervision, project administration, funding acquisition, writing - review & editing.

Editors: Eva Lantsoght, Daniel Cardoso.